

Component based model order reduction with mortar tied contact for nonlinear quasi-static mechanical problems

Stephan Ritzert^a, Jannick Kehls^a, Stefanie Reese^{a,b}, Tim Brepols^a

^a*Institute of Applied Mechanics, RWTH Aachen University,*

Mies-van-der-Rohe-Str. 1, 52074 Aachen, Germany

^b*University of Siegen, 57076 Siegen, Germany*

{stephan.ritzert, jannick.kehls, tim.brepols}@ifam.rwth-aachen.de

Abstract. In this work, we present a model order reduction technique for nonlinear structures assembled from components. The reduced order model is constructed by reducing the substructures with proper orthogonal decomposition and connecting them by a mortar-tied contact formulation. The snapshots for the substructure projection matrices are computed on the substructure level by the proper orthogonal decomposition (POD) method. The snapshots are computed using a random sampling procedure based on a parametrization of boundary conditions. To reduce the computational effort of the snapshot computation full-order simulations of the substructures are only computed when the error of the reduced solution is above a threshold. In numerical examples we show the accuracy and efficiency of the method for nonlinear problems involving material and geometric nonlinearity as well as non-matching meshes. We are able to predict solutions of systems that we did not compute in our snapshots.

Keywords: model-order reduction, nonlinear mechanics, substructuring, mortar method

1 Introduction

Many engineering structures are made of components. High-resolution finite element simulations of such systems are computationally expensive, especially for problems involving geometric and material nonlinearities. Model order reduction (MOR) can reduce this effort. In this work, we propose a method, where the reduced order model (ROM) of a nonlinear modular system is constructed from ROMs of the substructures.

The coupling of reduced substructures has a long history for linear dynamical systems. For an overview of the historical development of those methods, the reader is kindly referred to de Klerk et al. [2008]. A very popular component mode synthesis method is the Craig-Bampton method (Craig and Bampton [1968]), where the internal degrees of freedom (DOFs) are approximated by a combination of eigenmodes and so-called static constraint modes. The static constraint modes linearly relate the boundary DOFs to the internal DOFs and are computed by a static condensation of the stiffness matrix. Not many works exist that extend these component mode synthesis methods to nonlinear problems. For geometric nonlinearities, there exist works by Wenneker [2013], Kuether et al. [2016, 2017], and Bui et al. [2024] that extend the Craig-Bampton method (Craig and Bampton [1968]). In Kuether et al. [2016, 2017] a Craig-Bampton approximation of the displacement is used where the internal DOFs are reduced eigenmodes and static constraint modes. All of these quantities are computed from the linear stiffness matrix. Bui et al. [2024] enhanced the Craig-Bampton approach by static modal derivatives to account for the nonlinearity. In all of these works, the nonlinear force vector and stiffness matrix are approximated by cubic polynomial functions. This approximation is only valid for St. Venant-Kirchhoff materials and geometric nonlinearities. For large strains and nonlinear materials, the static constraint modes would also be a function of the displacement and would need to be updated in every Newton iteration. These methods only hold for small strains with large rotations because the static constraint modes are computed from the linear stiffness matrix.

In this work, we propose a data-driven reduction method where the DOFs of each substructure are reduced by the proper orthogonal decomposition (POD) method. We chose POD because it has proven to be an effective model order reduction method in nonlinear solid mechanics, see e.g. Herkt et al. [2009]; Radermacher and Reese [2013]. An overview of POD in the field of structural dynamics is given in Kerschen et al. [2005]. POD is also the foundation of more recent hyperreduction techniques applied to nonlinear mechanics, see among others: energy conserving sampling and weighting (Farhat et al. [2015]), discrete empirical interpolation method for nonlinear solid mechanics (Radermacher and Reese [2016]), (continuous) empirical cubature method (Hernández et al. [2017, 2024]), hyperreduction for nonlinear structural dynamics Rutzmoser [2018], hyperreduction for nonlinear computational homogenization problems (e.g. Guo et al. [2024]; Wulfinghoff [2024]).

Not many works use POD-based MOR in substructuring problems, where the ROM of the whole system is assembled from the ROMs of the components. For linear problems component-wise POD was used in Ritzert et al. [2023], where it was applied to parametric substructures and in McBane et al. [2022], where it was used for topology optimization of lattice-like structures. In nonlinear mechanics Zhou et al. [2018] proposed a method where the components are reduced by POD and connected by a penalty method. The penalty matrices are also reduced by parts of the substructure POD bases. In Hernández [2020] a method was proposed to compute periodic structures by another component-based MOR approach. In this approach, the substructures are

coupled by fictitious interfaces.

In this work, we propose a new approach. We use a mortar-tied contact formulation as a basis and reduce the degrees of freedom of the substructures by individual pre-computed POD bases. The mortar method is a state-of-the-art contact mechanics method for non-matching meshes. An advantage of the method is, that the Lagrange multipliers, as well as the slave-side DOFs, can be removed from the equation system by static condensation, by choosing dual shape functions for the Lagrange multipliers. This property is used in this MOR technique. For more information regarding the mortar method for tied-contact, the reader is referred to e.g. Wohlmuth [2001]; Puso [2004]; Laursen et al. [2012]; Popp and Wriggers [2018]. For the reduction, we split the DOFs of the substructures into internal and interface DOFs. Both internal and interface DOFs are reduced by projection matrices derived from POD bases of the whole substructure. The slave side interface DOFs are not reduced because they can be related to the reduced interface displacements of the master side.

In the numerical examples, we discuss the performance and accuracy of our method. We investigate large deformations, different stiffnesses of the substructures, non-matching meshes and viscoelastic material behavior. For all numerical examples, the snapshots are computed on the substructure level. We parametrize the displacement boundary conditions and use a random sampling procedure. In the proposed sampling procedure we only compute a full-order solution of a random sample point, if the sample point cannot already be represented by the substructure's current POD-basis.

Outline of the paper In Section 2, we first discuss the mortar tied-contact full order model (Section 2.1) and then explain the component-based model order reduction technique, where the substructures are first reduced and then connected by the reduced mortar tied-contact (Section 2.2). In Section 3, we present our method to compute snapshots. This method is based on a parametrization of boundary conditions and a randomized sampling scheme. The accuracy and performance of the MOR technique and the snapshot sampling method are investigated in the numerical examples in Section 4. Finally, the results are discussed in Section 5.

2 Component based model order reduction

2.1 Full-order model

The full-order model (FOM) from which we derive our reduced-order model (ROM) is a mortar-tied-contact formulation with static condensation of the Lagrange multipliers and the contact displacements on the slave side. In the following, it is briefly derived.

Weak formulation

In tied-contact, we introduce two conditions that have to be fulfilled in addition to the balance of linear momentum. The first condition is that the displacements of two bodies have to be equal on the contact interface $\Gamma_c^{1,2}$:

$$\mathbf{u}_c^1 = \mathbf{u}_c^2 \quad \text{on } \Gamma_c^{1,2} \quad (1)$$

The second condition is the equilibrium of the tractions acting on the two bodies at the contact interface:

$$-\mathbf{t}_c^1 = \mathbf{t}_c^2 \quad \text{on } \Gamma_c^{1,2} \quad (2)$$

A tied-contact problem consisting of two substructures is displayed in Figure 1.

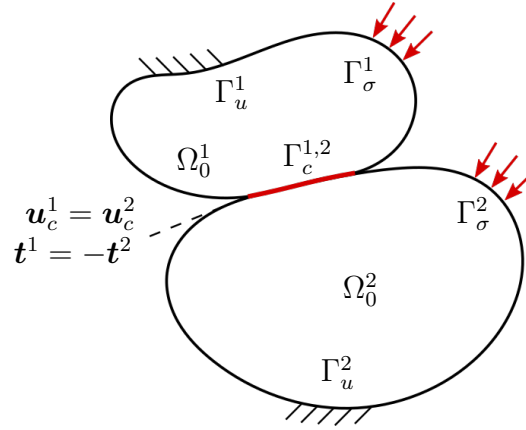


Figure 1: Illustration of a domain, that is composed of two subdomains Ω_0^1 and Ω_0^2 , with the Neumann boundary Γ_σ^1 and Dirichlet boundary Γ_u^2 . At the contact interface $\Gamma_c^{1,2}$, the two tied contact conditions are displayed.

In this work, we use the Lagrange multiplier method to enforce those conditions. We introduce the Lagrange multiplier $\boldsymbol{\lambda} = -\mathbf{t}_c^1 = \mathbf{t}_c^2$ and come up with the variational saddle-point problem, that can be derived from the Lagrange functional (see e.g. Wohlmuth [2001]):

$$\begin{aligned} \sum_{i=1}^{n_s} \delta g_{\text{int}}^i(\mathbf{u}, \delta \mathbf{u}) + \sum_{j=1}^{n_c} \delta g_{c,u}^j(\boldsymbol{\lambda}, \delta \mathbf{u}_c^1, \delta \mathbf{u}_c^2) &= 0 \\ \sum_{j=1}^{n_c} \delta g_{c,\lambda}^j(\mathbf{u}_c^1, \mathbf{u}_c^2, \delta \boldsymbol{\lambda}) &= 0 \end{aligned} \quad (3)$$

Here n_s is the number of substructures and n_c is the number of tied-contact interfaces. The displacements at the tied contact interfaces denoted by $\mathbf{u}_c^1, \mathbf{u}_c^2$ are subsets of the displacements of the respective substructures that share that interface. The weak form of the balance of linear momentum for the quasi-static case is

$$\delta g_{\text{int}}^i = \int_{\Omega_0} (\mathbf{S} : \delta \mathbf{E} - \rho \mathbf{b} \cdot \delta \mathbf{u}) dV - \int_{\Gamma_t} \delta \mathbf{u} \cdot \mathbf{t} dA, \quad (4)$$

where \mathbf{S} is the second Piola-Kirchhoff stress tensor, $\delta \mathbf{E}$ is the virtual Green-Lagrange strain tensor, \mathbf{b} are the body forces, ρ is the density and \mathbf{t} are the tractions acting on the boundary Γ_t . From the variational Lagrange multiplier method, we get the following contributions that enforce the tied-contact constraints

$$\delta g_{c,u}^j = \int_{\Gamma_c^{1,2}} (\delta \mathbf{u}_c^1 - \delta \mathbf{u}_c^2) \cdot \boldsymbol{\lambda} \, dA \quad (5)$$

$$\delta g_{c,\lambda}^j = \int_{\Gamma_c^{1,2}} \delta \boldsymbol{\lambda} \cdot (\mathbf{u}_c^1 - \mathbf{u}_c^2) \, dA \quad (6)$$

Discretization

To solve equation Equation (3), we discretize Equation (4) to Equation (6) with the finite element method (FEM). A displacement-based discretization of Equation (4) leads to the nonlinear $n \times 1$ -dimensional vector equation

$$\mathbf{G}(\mathbf{U}(t), t) = \mathbf{R}(\mathbf{U}(t)) - \mathbf{F}_{\text{ext}}(t). \quad (7)$$

$\mathbf{R}(\mathbf{U}(t))$ is the internal force vector, that depends nonlinearly on the displacement vector $\mathbf{R}(\mathbf{U}(t))$ at time t , and $\mathbf{F}_{\text{ext}}(t)$ is the external force vector. The discretization of Equation (5) and Equation (6) yields

$$\delta g_{c,u} = \delta(\mathbf{U}_c^1)^T \mathbf{D}^T \boldsymbol{\Lambda} - \delta(\mathbf{U}_c^2)^T \mathbf{M}^T \boldsymbol{\Lambda} \quad (8)$$

$$\delta g_{c,\lambda} = \delta \boldsymbol{\Lambda}^T \mathbf{D} \mathbf{U}_c^1 - \delta \boldsymbol{\Lambda}^T \mathbf{M} \mathbf{U}_c^2 \quad (9)$$

where we introduce the mortar-matrices \mathbf{D} and \mathbf{M} . These matrices arise from a finite element discretization of the interface displacements $\mathbf{u}_c^i = \mathbf{N}^i \mathbf{U}_c^i$ and the Lagrange multipliers $\boldsymbol{\lambda} = \hat{\mathbf{N}}^1 \boldsymbol{\Lambda}$. \mathbf{N}^1 and \mathbf{N}^2 are shape functions for the displacements and the coordinates of the slave and master side interface elements. $\hat{\mathbf{N}}^1$ are the shape functions of the Lagrange multiplier, defined on the slave side of the interface. The mortar matrices are computed for all n_e interface elements and assembled into the matrices \mathbf{D} , \mathbf{M} . They are defined as:

$$\mathbf{D} = \hat{\mathbf{A}}_{e=1}^{n_e} \mathbf{D}^e, \quad \mathbf{D}^e = \int_{\Gamma_e^1} (\hat{\mathbf{N}}^1)^T \mathbf{N}^1 \, dA \quad (10)$$

$$\mathbf{M} = \hat{\mathbf{A}}_{e=1}^{n_e} \mathbf{M}^e, \quad \mathbf{M}^e = \int_{\Gamma_e^1} (\hat{\mathbf{N}}^1)^T \mathbf{N}^2 \, dA. \quad (11)$$

The integrals on the element level can be solved by the mortar method (e.g. Puso [2004]; Popp and Wriggers [2018]). The advantage of this method is, that the integrals can be solved for non-conforming meshes.

The discretized equations for a system consisting of n_s substructures and n_c tied-contact inter-

faces reads

$$\sum_{i=1}^{n_s} \mathbf{G}_i(t, \mathbf{U}_i) + \sum_{j=1}^{n_c} (\mathbf{D}_j^T \boldsymbol{\Lambda}_j - \mathbf{M}_j^T \boldsymbol{\Lambda}_j) = 0 \quad (12)$$

$$\sum_{j=1}^{n_c} (\mathbf{D}_j \mathbf{U}_{c,j}^1 - \mathbf{M}_j \mathbf{U}_{c,j}^2) = 0 \quad (13)$$

Note, that the displacements of each contact interface j : $\mathbf{U}_{c,j}^1$ and $\mathbf{U}_{c,j}^2$ are a subset of the displacements of a substructure \mathbf{U}_i . Since $\mathbf{G}_i(t, \mathbf{U}_i)$ is a nonlinear vector, the above system of equations (Equations (12) and (13)) will be solved by the Newton-Raphson scheme. For the linearization of Equation (12) we define the tangential stiffness matrix of a substructure i for the displacement state \mathbf{U}_i^k as $\mathbf{K}_i(\mathbf{U}_i^k) := \frac{\partial \mathbf{G}_i}{\partial \mathbf{U}_i} |_{\mathbf{U}_i^k}$. To compute the solution of the $k+1$ iteration we solve the following equation system for all $\Delta \mathbf{U}_i$

$$\sum_{i=1}^{n_s} (\mathbf{G}_i(t, \mathbf{U}_i^k) + \mathbf{K}_i(\mathbf{U}_i^k) \Delta \mathbf{U}_i) + \sum_{j=1}^{n_c} (\mathbf{D}_j^T \boldsymbol{\Lambda}_j^k - \mathbf{M}_j^T \boldsymbol{\Lambda}_j^k) = 0 \quad (14)$$

$$\sum_{j=1}^{n_c} (\mathbf{D}_j \Delta \mathbf{U}_{c,j}^1 - \mathbf{M}_j \Delta \mathbf{U}_{c,j}^2) = 0 \quad (15)$$

The displacements of all substructures are then updated by $\mathbf{U}_i^{k+1} = \mathbf{U}_i^k + \Delta \mathbf{U}_i$. This procedure is repeated until Equations (12) and (13) are approximately fulfilled.

For simplicity, further derivations are shown for a system with two substructures, where one body is called master and the other is called slave. From now on, the master degrees of freedom will be denoted by a superscript M and the slave degrees of freedom by a superscript S . The displacements and residual vectors of each substructure are split into internal degrees of freedom \mathbf{U}_I , \mathbf{G}_I and tied contact degrees of freedom \mathbf{U}_C , \mathbf{G}_C . The tangential stiffness matrices are split accordingly into four block matrices. For this special case, Equations (14) and (15) can be written in matrix-vector notation:

$$\begin{bmatrix} \mathbf{K}_{II}^M & \mathbf{0} & \mathbf{K}_{IC}^M & \mathbf{0} & \mathbf{0} \\ \mathbf{0} & \mathbf{K}_{II}^S & \mathbf{0} & \mathbf{K}_{IC}^S & \mathbf{0} \\ \mathbf{K}_{CI}^M & \mathbf{0} & \mathbf{K}_{CC}^M & \mathbf{0} & -\mathbf{M}^T \\ \mathbf{0} & \mathbf{K}_{CI}^S & \mathbf{0} & \mathbf{K}_{CC}^S & \mathbf{D}^T \\ \mathbf{0} & \mathbf{0} & -\mathbf{M} & \mathbf{D} & \mathbf{0} \end{bmatrix} \begin{bmatrix} \Delta \mathbf{U}_I^M \\ \Delta \mathbf{U}_I^S \\ \Delta \mathbf{U}_C^M \\ \Delta \mathbf{U}_C^S \\ \boldsymbol{\Lambda} \end{bmatrix} = - \begin{bmatrix} \mathbf{G}_I^M \\ \mathbf{G}_I^S \\ \mathbf{G}_C^M \\ \mathbf{G}_C^S \\ \mathbf{0} \end{bmatrix} \quad (16)$$

This equation system is indefinite, due to the zero block matrix on the main diagonal associated with the Lagrange multipliers. This structure is unfavorable for efficient solution algorithms. It requires special preconditioning techniques to apply iterative solution methods like the conjugate gradient (CG), or the generalized minimal residual (GMRES) method (Saad [2003]). Moreover, the additional degrees of freedom would require additional mode matrices for the ROM. In this paper, we use the mortar method to compute the matrices \mathbf{D} and \mathbf{M} (Wohlmuth

[2001]; Laursen et al. [2012]; Popp and Wriggers [2018]). The advantage of this method is, that the Lagrange multipliers can be removed from the system of equations in Equation (16), and it can be transformed into a symmetric positive definite system of equations. Another advantage is the integration procedure to compute the mortar matrices \mathbf{D} and \mathbf{M} , which allows for non-conforming meshes. The integration procedure is explained in detail in e.g. Puso [2004]; Popp and Wriggers [2018].

Static condensation

In this section, we describe how the system of equations in Equation (16) can be transformed into a symmetric positive definite system by static condensation. From the fifth equation of Equation (16) it follows:

$$\Delta U_C^S = \mathbf{D}^{-1} \mathbf{M} \Delta U_C^M := \mathbf{P} \Delta U_C^M \quad (17)$$

where $\mathbf{P} := \mathbf{D}^{-1} \mathbf{M}$ is the discrete interface coupling operator (Popp and Wriggers [2018]). The Lagrange multipliers Λ can be expressed as

$$\Lambda = \mathbf{D}^{-T} (-\mathbf{g}_c^S - \mathbf{K}_{CI}^S \Delta U_I^S - \mathbf{K}_{CC}^S \Delta U_C^S) \quad (18)$$

by reordering the fourth equation of the equation system given in Equation (16). By inserting Equation (18) into the second and third equation of Equation (16) and utilizing Equation (17) we obtain the final condensed system of equations:

$$\underbrace{\begin{bmatrix} \mathbf{K}_{II}^M & \mathbf{0} & \mathbf{K}_{IC}^M \\ \mathbf{0} & \mathbf{K}_{II}^S & \mathbf{K}_{IC}^S \mathbf{P} \\ \mathbf{K}_{CI}^M & \mathbf{P}^T \mathbf{K}_{CI}^S & \mathbf{K}_{CC}^M + \mathbf{P}^T \mathbf{K}_{CC}^S \mathbf{P} \end{bmatrix}}_{\mathbf{K}_{\text{cond}}} \underbrace{\begin{bmatrix} \Delta U_I^M \\ \Delta U_I^S \\ \Delta U_C^M \end{bmatrix}}_{\Delta U_{\text{cond}}} = - \underbrace{\begin{bmatrix} \mathbf{G}_I^M \\ \mathbf{G}_I^S \\ \mathbf{G}_C^M + \mathbf{P}^T \mathbf{G}_C^S \end{bmatrix}}_{\mathbf{G}_{\text{cond}}} \quad (19)$$

Here also the definition of the interface coupling operator $\mathbf{P} := \mathbf{D}^{-1} \mathbf{M}$ is used. This static condensation requires the inversion of the mortar matrix \mathbf{D} , which for standard shape functions is computationally expensive. A solution to this problem was proposed by Wohlmuth [2001] by choosing dual shape functions for the Lagrange multipliers. Because of these dual shape functions, the mortar matrix \mathbf{D} reduces to a diagonal matrix that can be easily inverted.

The dual Lagrange multiplier shape functions \hat{N}_j^S are defined by the biorthogonality condition with the displacement shape functions N_k^S :

$$\int_{\Gamma_e} \hat{N}_j^S N_k^S \, dA = \delta_{jk} \int_{\Gamma_e} N_k^S \, dA \quad (20)$$

which was first presented in the works of Scott and Zhang [1990] and applied to the mortar method in Wohlmuth [2001]. The Lagrange multiplier shape functions are computed by a linear mapping of the standard displacement shape functions

$$\hat{N}_j^S = a_{jk} N_k^S \quad (21)$$

with the coefficient matrix $\mathbf{A} = [a_{jk}]$. The coefficients are obtained by the expression

$$\mathbf{A} = \mathbf{B}\mathbf{C}^{-1}, \quad (22)$$

stemming from the biorthogonality condition Equation (20). The entries of the matrices $\mathbf{B} = [b_{jk}]$ and $\mathbf{C} = [c_{jk}]$ are computed by

$$b_{jk} = \delta_{jk} \int_{\Gamma_e} N_k \, dA \quad (23)$$

$$c_{jk} = \int_{\Gamma_e} N_j N_k \, dA. \quad (24)$$

With the method described above, the condensed system of equations can be efficiently computed. It should be noted, that the interface-coupling operator \mathbf{P} only needs to be computed in the beginning. Only the residual vectors and tangential stiffness matrices of the substructures have to be evaluated in every iteration step. The condensed system of equations Equation (19) is the basis of the reduced-order model described in the following section.

2.2 Reduced-order model

Component based model order reduction

The idea of this model order reduction (MOR) technique is to reduce the DOFs of the substructures on their own and assemble them into a global reduced system of equations. The difference to the MOR techniques in Zhou et al. [2018]; Ritzert et al. [2023] is that we here use the mortar method for mesh-tying (cf. Section 2.1) instead of the penalty approach.

For the derivation of the ROM, we use a system composed of two substructures denoted by the superscripts S for the slave side and M for the master side (cf. Equation (16) to Equation (19)). The displacement vectors of the substructures are split into internal displacements $\mathbf{U}_I^{S,M}$ with $n_I^{S,M}$ degrees of freedom and interface displacements $\mathbf{U}_C^{S,M}$ with $n_C^{S,M}$ degrees of freedom. The displacements of the master side are approximated by the product

$$\mathbf{U}^M = \begin{bmatrix} \mathbf{U}_I^M \\ \mathbf{U}_C^M \end{bmatrix} \approx \begin{bmatrix} \mathbf{\Psi}_I^M & \mathbf{0} \\ \mathbf{0} & \mathbf{\Psi}_C^M \end{bmatrix} \begin{bmatrix} \mathbf{a}_I^M \\ \mathbf{a}_C^M \end{bmatrix} \quad (25)$$

where $\mathbf{\Psi}_I^M$ and $\mathbf{\Psi}_C^M$ are orthonormal projection matrices with the dimensions $n_I^M \times m_I^M$ and $n_C^M \times m_C^M$, respectively. The vectors \mathbf{a}_I^M and \mathbf{a}_C^M contain the m_I^M and m_C^M reduced displacements of the master substructure. By choosing the projection matrix $\mathbf{\Psi}_C^M = \mathbf{I}$ as an $n_C^M \times n_C^M$ -dimensional identity matrix one obtains a system where only the internal degrees of freedom are reduced. This can be in some cases advantageous, but in most examples throughout this

paper, the contact degrees of freedom are reduced. The product

$$\mathbf{U}^S = \begin{bmatrix} \mathbf{U}_I^S \\ \mathbf{U}_C^S \end{bmatrix} \approx \begin{bmatrix} \Psi_I^S & \mathbf{0} \\ \mathbf{0} & \mathbf{I} \end{bmatrix} \begin{bmatrix} \mathbf{a}_I^S \\ \mathbf{U}_C^S \end{bmatrix} \quad (26)$$

approximates the slave-side displacements. Here, only the internal DOFs are approximated by the $n_I^S \times m_I^S$ -dimensional projection matrix Ψ_I^S and the corresponding unknowns \mathbf{a}_I^S . The slave-side interface displacements \mathbf{U}_C^S are not approximated since they can be expressed in terms of the interface-coupling operator \mathbf{P} and the approximation of the master-side displacements \mathbf{U}_C^M (cf. Equation (17))

$$\mathbf{U}_C^S = \mathbf{P} \Psi_C^M \mathbf{a}_C^M \quad (27)$$

Inserting the relations Equation (25), Equation (26) and Equation (27) into the condensed equation system Equation (19) and applying a Galerkin projection with the projection matrices Ψ_I^M , Ψ_I^S and Ψ_C^M of the corresponding degrees of freedom. In the Galerkin projection we multiply the transposed projection matrices from the left side to the corresponding degrees of freedom. This leads to the reduced quantities:

$$\bar{\mathbf{K}}_{\text{cond}} = \begin{bmatrix} (\Psi_i^M)^T \mathbf{K}_{ii}^M \Psi_i^M & \mathbf{0} & (\Psi_i^M)^T \mathbf{K}_{ic}^M \Psi_c^M \\ \mathbf{0} & (\Psi_i^S)^T \mathbf{K}_{ii}^S \Psi_i^S & (\Psi_i^S)^T \mathbf{K}_{ic}^S \mathbf{P} \Psi_c^M \\ (\Psi_c^M)^T \mathbf{K}_{ci}^M \Psi_i^M & (\Psi_c^M)^T \mathbf{P}^T \mathbf{K}_{ci}^S \Psi_i^S & (\Psi_c^M)^T (\mathbf{K}_{cc}^M + \mathbf{P}^T \mathbf{K}_{cc}^S \mathbf{P}) \Psi_c^M \end{bmatrix} \quad (28)$$

$$\Delta \mathbf{a}_{\text{cond}} = \begin{bmatrix} \Delta \mathbf{a}_i^M \\ \Delta \mathbf{a}_i^S \\ \Delta \mathbf{a}_c^M \end{bmatrix} \quad (29)$$

$$\bar{\mathbf{G}}_{\text{cond}} = \begin{bmatrix} (\Psi_i^M)^T \mathbf{G}_i^M \\ (\Psi_i^S)^T \mathbf{G}_i^S \\ (\Psi_c^M)^T (\mathbf{G}_c^M + \mathbf{P}^T \mathbf{G}_c^S) \end{bmatrix} \quad (30)$$

The Lagrange Multipliers can be computed from the reduced displacements by

$$\Lambda = \mathbf{D}^{-T} (-\mathbf{G}_C^S - \mathbf{K}_{CI}^S \Psi_I^S \Delta \mathbf{a}_I^S - \mathbf{K}_{CC}^S \mathbf{P} \Psi_C^M \Delta \mathbf{a}_C^M). \quad (31)$$

The discrete nonlinear system of reduced equations is solved by the Newton-Raphson method. The iterative solution algorithm for a timestep is shown in Algorithm 1

Comment It should be noted, that for every iteration the residuals \mathbf{G}_S , \mathbf{G}_M and the tangential stiffness matrices \mathbf{K}_S , \mathbf{K}_M have to be computed for every substructure. The computational effort to solve the system is reduced but the computation of those matrices still depends on the original problem size $n = n_M + n_S$. At this stage hyperreduction techniques could be used to reduce this effort even further. In nonlinear solid mechanics the discrete empirical interpolation method (DEIM) (see Chaturantabut and Sorensen [2010]; Radermacher and Reese [2016])

Algorithm 1: Newton-Raphson solution of the nonlinear modular system

```

while  $\|\hat{\mathbf{G}}_{\text{cond}}(\mathbf{U}_j^M, \mathbf{U}_j^S)\| > \text{tol.}$  do
   $\Delta \mathbf{a} = - \left( \hat{\mathbf{K}}_{\text{cond}}(\mathbf{U}_j^M, \mathbf{U}_j^S) \right)^{-1} \hat{\mathbf{G}}_{\text{cond}}(\mathbf{U}_j^M, \mathbf{U}_j^S)$ 
   $\mathbf{U}_{j+1}^M = \mathbf{U}_j^M + \begin{bmatrix} \Psi_I^M \Delta \mathbf{a}_I^M \\ \Psi_C^M \Delta \mathbf{a}_C^M \end{bmatrix}$ 
   $\mathbf{U}_{j+1}^S = \mathbf{U}_j^S + \begin{bmatrix} \Psi_I^S \Delta \mathbf{a}_I^S \\ \mathbf{P} \Psi_C^M \Delta \mathbf{a}_C^M \end{bmatrix}$ 
   $j \leftarrow j + 1$ 

```

), (continuous) empirical cubature (Hernández et al. [2017, 2024]), or energy conserving sampling and weighting (ECSW) (Farhat et al. [2015]; Rutzmoser [2018]) proved to be well suited. However, having a working POD-based model order reduction is a necessary step towards hyperreduced component-based model order reduction. The extension to hyperreduction is out of the scope of this paper but will be addressed in future works.

Proper orthogonal decomposition

In the previous paragraph, we introduced the projection matrices Ψ_I^M , Ψ_C^M , and Ψ_I^S but have not mentioned yet how they can be computed. We use the proper orthogonal decomposition (POD) method to compute the projection matrices since it showed good results for nonlinear mechanics simulations (Radermacher and Reese [2013]; Rutzmoser [2018]). In POD, the projection matrix is computed from collected data of l displacement states of the substructure, the so-called snapshots. The snapshots are stored in a matrix

$$\mathbf{S}_{\text{Snap}} = [\mathbf{U}_1, \mathbf{U}_2, \dots, \mathbf{U}_l] = \Phi \Theta \Omega \quad (\text{SVD}) \quad (32)$$

which can be decomposed by a singular value decomposition (SVD) into the left and right mode matrix Φ and Ω , respectively, as well as the singular values Θ . The projection matrix is constructed by selecting only the first m columns of Φ . Leading to the $n^s \times m$ dimensional projection matrix

$$\Psi = [\Phi_1, \dots, \Phi_m], \quad (33)$$

where n^s is the number of DOFs of the substructure. The projection matrices for the internal DOFs Ψ_I^M and Ψ_I^S or interface DOFs Ψ_C^M are obtained by selecting the corresponding DOFs of the projection matrix of a substructure.

3 Computation of snapshots

In this work, we compute the snapshots on the substructure level. The snapshots should produce modes that are general enough to be used in different structures. This is done by parameterizing the boundary conditions applied on the possible interface surfaces. These parameters are stored in the vector $\boldsymbol{\alpha} = [\alpha_1, \alpha_2, \dots, \alpha_k]$. A snapshot can be computed by solving the nonlinear FEM problem $\mathbf{G}(\mathbf{U}, \boldsymbol{\alpha}) = \mathbf{0}$, by the Newton-Raphson method. The goal is now to find a POD basis $\boldsymbol{\Psi}$, such that $\|\mathbf{G}(\boldsymbol{\Psi}\mathbf{a}, \boldsymbol{\alpha})\|_2 < \varepsilon$, for the whole parameter space $\boldsymbol{\alpha}$. Here $\|\bullet\|_2$ denotes the L_2 norm of \bullet and ε is a tolerance. We assume, that if this condition is fulfilled we have found a basis, that works in global structures. This assumption is only valid if the parameterization is well-chosen.

For such parameter sampling problems, popular methods use a greedy approach to select parameters where displacement states are computed (see e.g. Bui-Thanh et al. [2008] or Haasdonk and Ohlberger [2008]). In the following, we will refer to these parameters as sample points. In these approaches, the projection matrix is updated in every iteration by selecting a new sampling point and computing new snapshots there. The sampling point is chosen by solving an optimization problem to find the parameter point with the largest error. An overview of parametric model order reduction is given in Benner et al. [2015].

In this work, we choose a different approach, where the new sampling points are chosen randomly. At every random sampling point, we first compute the reduced solution and check the error criterion: $\|\mathbf{G}(\boldsymbol{\Psi}\mathbf{a}, \boldsymbol{\alpha})\| < tol$. If the error criterion is not fulfilled, we compute the full solution at this sample point and update the projection matrix. The new number of modes is computed by a bisection scheme, such that $\|\mathbf{G}(\boldsymbol{\Psi}\mathbf{a}, \boldsymbol{\alpha})\| \approx \varepsilon$. The algorithm is shown in alg. 2. This simple approach was chosen because it already gives sufficient results and does not require solving an optimization problem.

After the sampling procedure is finished, the mode matrix is computed from the resulting snapshot matrix. The mode matrix that is used during the sampling is only used to check if the current sampling point is already captured by the current modes.

Algorithm 2: Sampling procedure

Input: initial snapshot matrix: $\mathcal{S}_{\text{Snap}}$

initial projection matrix: Ψ with m modes

Output: snapshot matrix: $\mathcal{S}_{\text{Snap}}$

for $k \in \{1, \dots, n_{\text{samples}}\}$ **do**

 compute random sampling point α_k

 compute the reduced solution: solve $\Psi^T \mathbf{G}(\Psi \mathbf{a}, \alpha_k) = \mathbf{0}$

if $\|\mathbf{G}(\Psi \mathbf{a}, \alpha)\| \geq \varepsilon$ **then**

 compute new snapshots: solve $\mathbf{G}(\mathbf{U}, \alpha_k) = \mathbf{0} \rightarrow \mathbf{U}$

 update snapshot matrix: $\mathcal{S}_{\text{Snap}} \leftarrow [\mathcal{S}_{\text{Snap}}, \mathbf{U}]$

 compute SVD: $\mathcal{S}_{\text{Snap}} = \Phi \Theta \Omega$

 compute the new number of modes by bisection method, such that

$\|\mathbf{G}(\Psi \mathbf{a}, \alpha)\| \approx \varepsilon \rightarrow m$

 compute new mode matrix with m modes: $\Psi = [\Phi_1, \dots, \Phi_m]$

4 Numerical Examples

4.1 Example 1

4.1.1 Boundary value problem

In this numerical example, we use the same geometry in two different systems. The first system consists of 6 substructures and is displayed in Figure 2. The substructure in the bottom right corner has a finer mesh than the other substructures. In total, the system has 29358 DOFs. Each substructure is characterized by a Neo-Hookean material behavior with a Young's modulus of $E = 80$ GPa and a Poisson's ratio of $\nu = 0.15$. Additionally to this nonlinear material behavior, we also consider geometric nonlinearities by employing finite strain theory. The boundary conditions and dimensions can be taken from Figure 2. The maximum displacement applied to the system is $\bar{u}_x^{\max} = 30$ mm.

The second system consists of 9 substructures and is displayed in Figure 3. Here, all substructures have the same mesh but the substructures marked in blue have a higher stiffness than the grey substructures. The blue substructures have a Young's modulus of $E = 80$ GPa, the grey substructures of $E = 20$ GPa, and all substructures have the same Poisson's ratio $\nu = 0.15$. The system has in total 36990 DOFs. The boundary conditions and dimensions can be taken from Figure 3. We apply a displacement in y -direction on the whole right surface, while fixing the x -displacement on that side.

For the reduced simulations we use the same set of snapshots for all substructures.

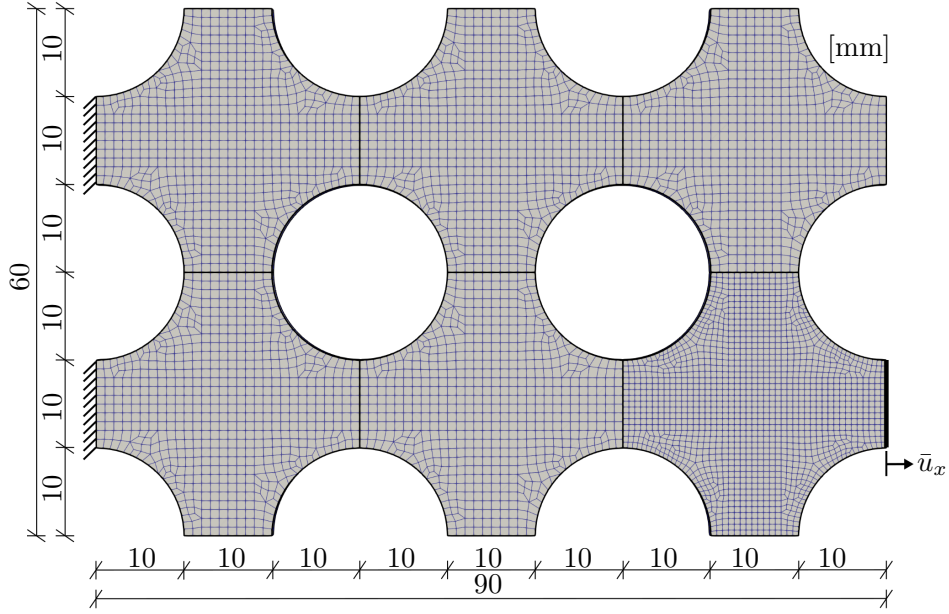


Figure 2: Geometry, mesh and boundary conditions of the 2×3 example. The substructure on the bottom right has a finer mesh than the other substructures.

4.1.2 Snapshot computation

The snapshots are computed on the substructure level. We parametrize the displacements on the left, right, top, and bottom by two parameters each. On the left and right edges, we prescribe the displacements in the x -direction. The snapshot parametrization is illustrated in Figure 4. The prescribed displacements \mathbf{U}_{BC}^l and \mathbf{U}_{BC}^r on the boundary depend on the parameters d_x^l and d_x^r describing a translation of the surfaces and the parameters φ_z^l and φ_z^r describing a rotation. On the top and bottom edges, we only prescribe the displacements in y -direction. We consider translation by the parameters d_y^t and d_y^b and rotation of the edges by the parameters φ_z^t and φ_z^b .

The normal distributed random parameters are chosen from the following parameter ranges:

$$\begin{aligned}
 d_x^l &\in (-10, 4) \text{ [mm]} & \varphi_z^l &\in (-35, 35) \text{ [}^\circ\text{]} \\
 d_x^r &\in (-4, 10) \text{ [mm]} & \varphi_z^r &\in (-35, 35) \text{ [}^\circ\text{]} \\
 d_y^b &\in (-10, 4) \text{ [mm]} & \varphi_z^b &\in (-35, 35) \text{ [}^\circ\text{]} \\
 d_y^t &\in (4, 10) \text{ [mm]} & \varphi_z^t &\in (-35, 35) \text{ [}^\circ\text{]}
 \end{aligned} \tag{34}$$

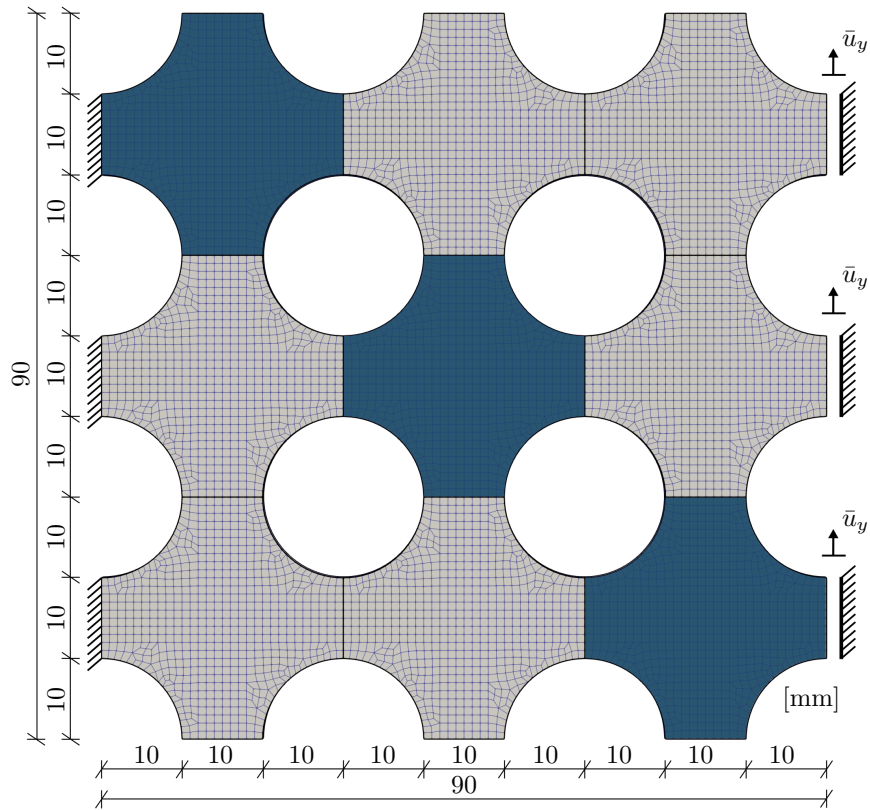


Figure 3: Geometry, mesh and boundary conditions of the 3×3 example. The blue substructures have a Young's modulus of $E = 80$ GPa, the grey substructures of $E = 20$ GPa.

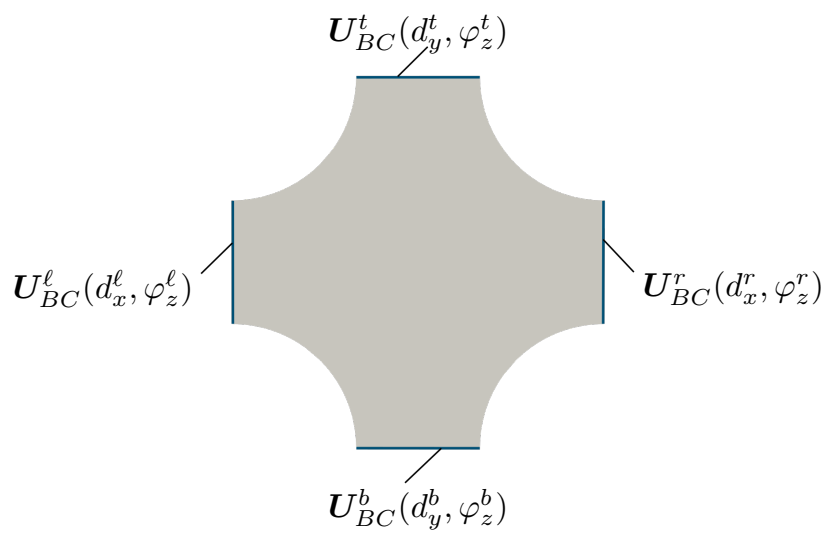


Figure 4: Illustration of the snapshot parametrization.

4.1.3 Simulation

In Figure 5 and Figure 6 we show the shear stress contour plots as well as the displacements of the two systems. The black outline is the outline of the reference solution computed by the mortar tied-contact method without model order reduction. In both figures, it can be seen that the displacements of the reduced solutions are in very good agreement with the reference solutions.

For the reduced solution of the system with 2×3 substructures 90 modes per substructure and 20 per interface are used. The system has approximately 43 times fewer DOFs than the reference solution $\left(\frac{29358}{680} \approx 43\right)$. The results from Figure 5 show further, that non-matching meshes are possible to solve with the ROM.

For the reduced solution of the system with 3×3 substructures 50 modes per substructure and 20 per interface are used. The system has approximately 53 times fewer DOFs than the reference solution $\left(\frac{36990}{690} \approx 53\right)$. Compared to the 2×3 system fewer modes per substructure are needed to get a reduced solution that is in good agreement with the reference solution. It can also be seen, that the modes computed with the method described in Section 3 can be used for different stiffnesses of the substructures.

In Figure 7 we show normalized force-displacement diagrams of the two load cases. For the system consisting of 2×3 substructures it can be seen that with 90 modes per substructure and 20 modes per interface, the reference solution can be matched. For the system with 3×3 substructures, the reaction forces of the reduced solution are overestimated. By increasing the number of modes of the substructure the reaction forces converge to the reference solution. A reason for the overestimation could be that the snapshots are computed with a Young's modulus of $E = 80$ GPa and the softer substructures have a Young's modulus of $E = 20$ GPa.

4.2 Example 2: Ring-segment

4.2.1 Boundary value problem

In this numerical example, we use the same substructure in two different systems. The dimensions and mesh of the component is shown in Figure 9. The boundary value problems are illustrated in Figure 8. On the left, four components are assembled into a ring structure, with 15876 DOFs in total. The other system consists of five substructures with 19845 DOFs. The displacement boundary conditions can be seen in Figure 8. In the following, we use the term "ring"-structure for the example on the left and the term "omega" for the structure shown on the right.

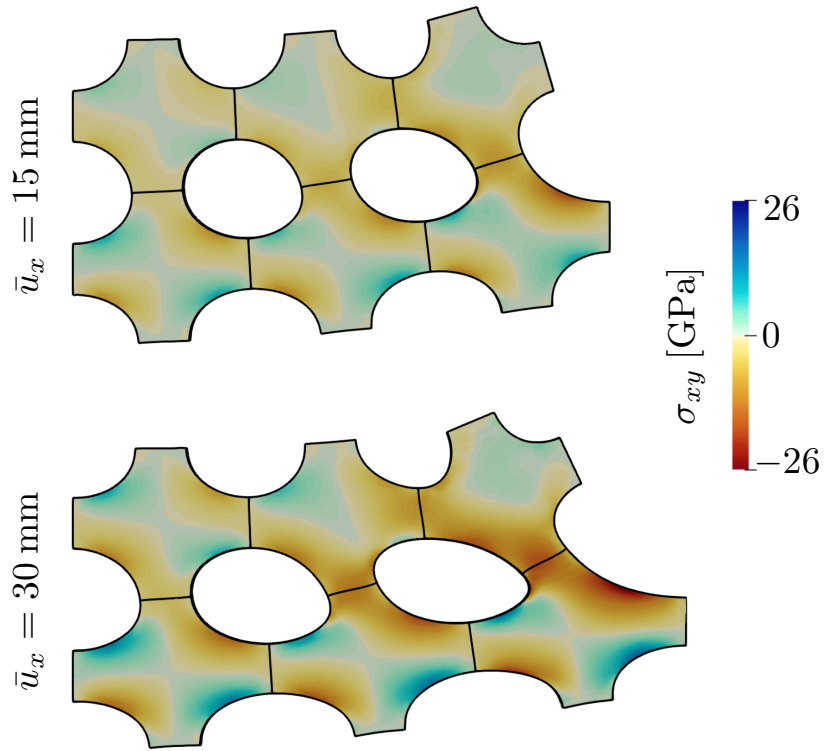


Figure 5: Cauchy shear stress contour plots of the deformed reduced solution. The black outlines are the reference solutions.

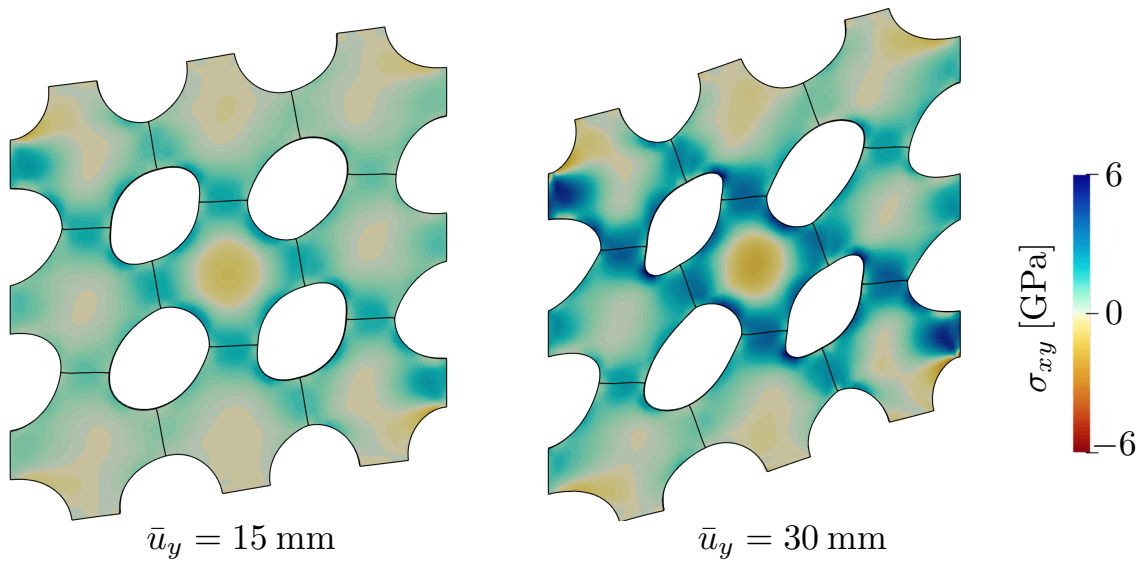


Figure 6: Cauchy shear stress contour plots of the deformed reduced solution. The black outlines are the reference solutions.

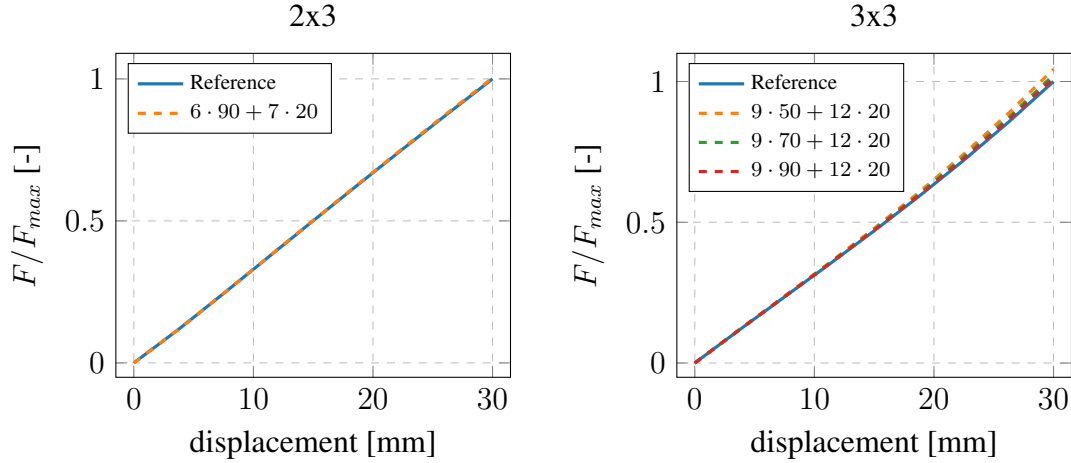


Figure 7: Plot of the reaction forces over the displacements for the 2×3 and 3×3 example.

In Section 4.2.3 the results for a Neo Hookean material and in Section 4.2.4 the results for a finite strain viscoelasticity model are shown.

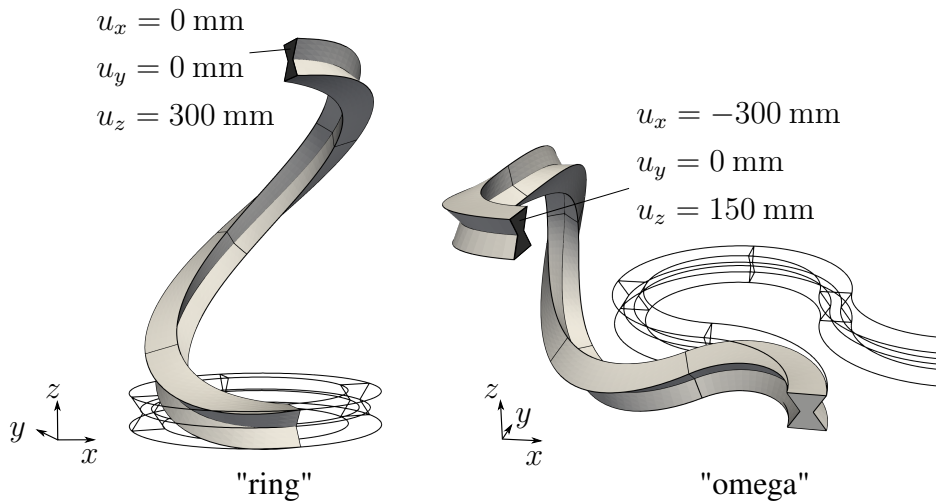


Figure 8: Boundary value problems of two systems "ring" and "omega", that are assembled from the same modules. For both systems, the undeformed configuration is shown as an outline, and the deformed configuration is shown in gray. Both systems are fixed where the deformed and the undeformed configurations coincide. The displacement boundary conditions are applied to the marked area.

In Figure 9 we show the meshes of the module used in the numerical examples from Figure 8.

4.2.2 Snapshot computation

The snapshots are computed for the substructure in the middle with the boundary value problem shown in Figure 10. The two substructures, that are attached left and right are used to apply the

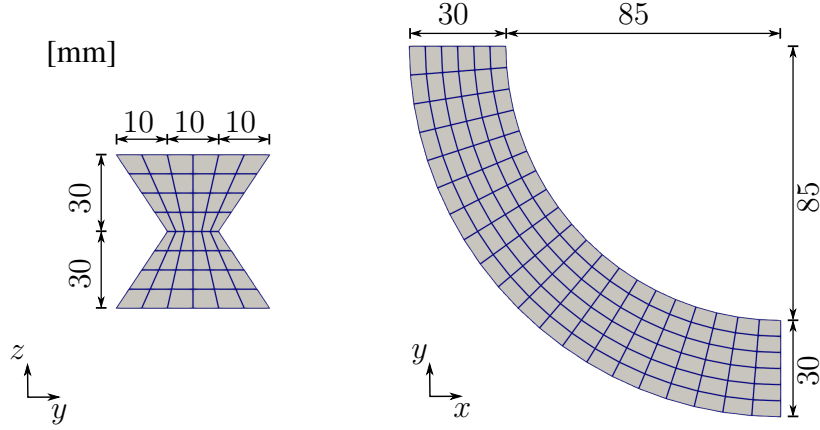


Figure 9: Geometry and mesh of a module. Crosssection (left) and topview (right)

boundary conditions on the surfaces $\Gamma_{\bar{u}}^1$ and $\Gamma_{\bar{u}}^2$. For the reduced computation in the sampling procedure shown in Algorithm 2, only the central substructure is reduced. The two blocks on the outside are unreduced.

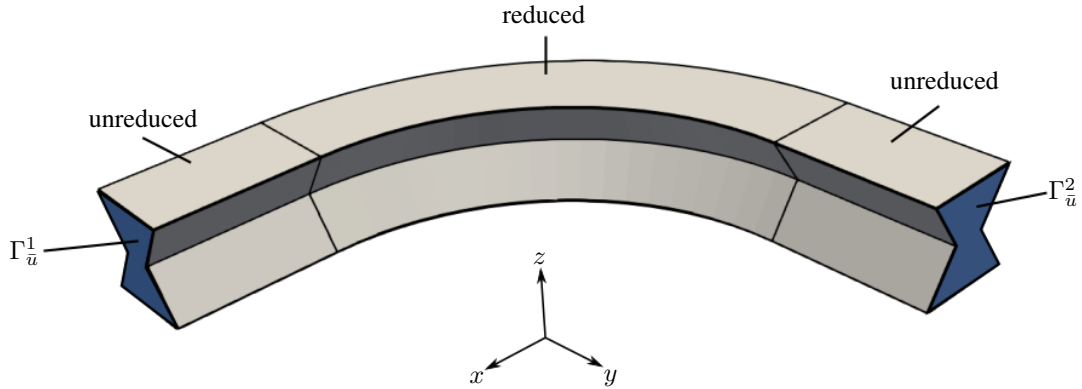


Figure 10: Boundary value problem for the snapshot computation, consisting of three substructures. The snapshots are collected for the central substructure.

On both surfaces, we apply a displacement that depends on six parameters $\mathbf{U}_{BC} = \mathbf{U}_{BC}(d_x, d_y, d_z, \varphi_x, \varphi_y, \varphi_z)$. The parameters d_x, d_y, d_z describe a displacement of the surface in x, y, z -direction. The parameters $\varphi_x, \varphi_y, \varphi_z$ rotate the surfaces $\Gamma_{\bar{u}}^1$ and $\Gamma_{\bar{u}}^2$ around the x, y, z -axes. The normal distributed random parameters are chosen from the following parameter ranges

$$\begin{aligned}
 d_x &\in (-80, 80) \text{ [mm]} & \varphi_x &\in (-60, 60) \text{ [}^\circ\text{]} \\
 d_y &\in (-30, 30) \text{ [mm]} & \varphi_y &\in (-60, 60) \text{ [}^\circ\text{]} \\
 d_z &\in (-100, 100) \text{ [mm]} & \varphi_z &\in (-15, 15) \text{ [}^\circ\text{]}
 \end{aligned} \tag{35}$$

For each random parameter point, we compute two snapshots. One where we apply the displacement to the surface $\Gamma_{\bar{u}}^1$ and set all displacement of the surface $\Gamma_{\bar{u}}^2$ to zero, and a second one

where the same displacement is applied to $\Gamma_{\bar{u}}^2$.

The projection matrices used in the following example are computed with 100 sample points, with 3 load steps each. We use a Neo-Hookean material model with the Lamé constants: $\lambda = 14907$ MPa, $\mu = 34783$ MPa.

4.2.3 Neo-Hooke material

The displacements and shear stresses σ_{xy} of the "ring"- and "omega" structure are shown in Figures 11 and 12. In both figures, the black outline is the displacement of the reference solution. It can be seen that the reduced solutions are in good agreement with the reference solution. The "ring" structure is computed with 80 modes per substructure and 40 modes per interface. This leads to a ROM with approximately 36 times fewer DOFs than the reference solution $\left(\frac{15876}{440} \approx 36\right)$. For the "omega" structure we used 120 modes per substructure and 40 modes per interface. Compared to the reference solution these are approximately 26 times fewer DOFs $\left(\frac{19845}{760} \approx 26\right)$. For both examples, the same snapshots are used to compute the mode matrices. This shows, that the snapshots computed with the method described above can be used in different boundary value problems.

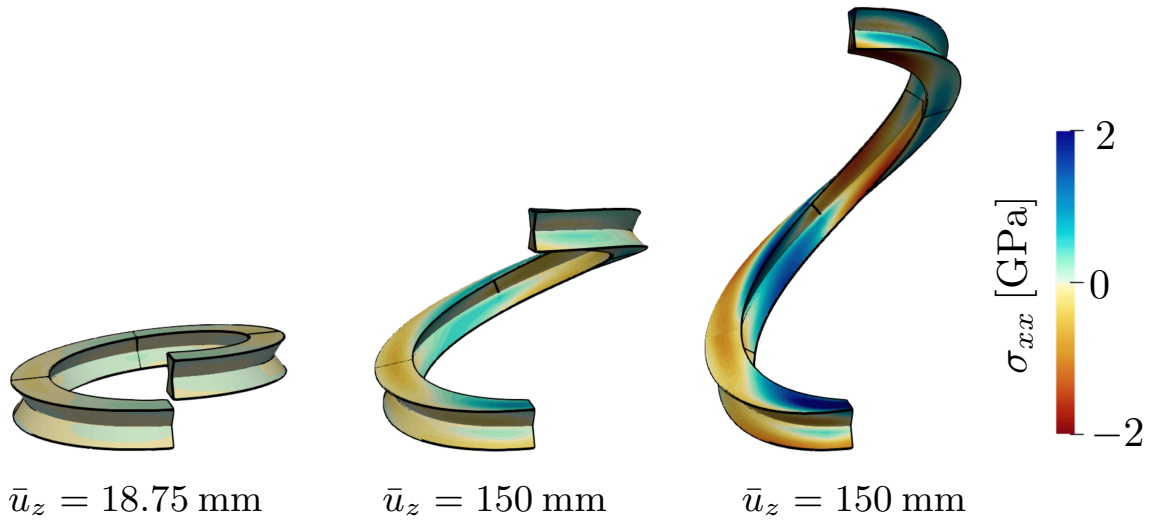


Figure 11: Shear stress contour plots of the deformed reduced solution of the "ring" boundary value problem. The black outline is the reference solution.

In the following, we analyze the reaction force-displacement curves for the two examples. We also compare the method to the penalty approach proposed in Zhou et al. [2018].

For the "ring" structure the reaction force-displacement curves for the mortar MOR approach and the penalty method are shown in Figure 13. It can be seen that the reaction forces of the

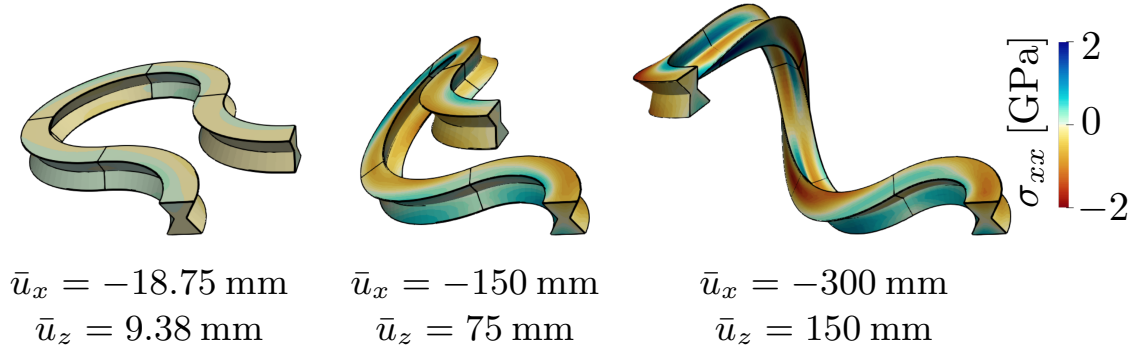


Figure 12: Shear stress contour plots of the deformed reduced solution of the "omega" boundary value problem. The black outline is the reference solution.

mortar MOR method are in good agreement with the reference solution. The reduced solution with the penalty approach underestimates the reaction forces. For 60 DOFs the curves match, but when the number of modes is increased the reaction forces converge to wrong values. The reason is that the penalty parameter influences the solution. If the penalty parameter is too high, the reaction forces are overestimated. For too small values the reaction forces are underestimated. In this example, the penalty parameter is chosen as $\varepsilon = 10^3$. For this parameter, we needed 10 times more load steps to get convergence, for higher penalty parameters the reduced solution did not converge at all.

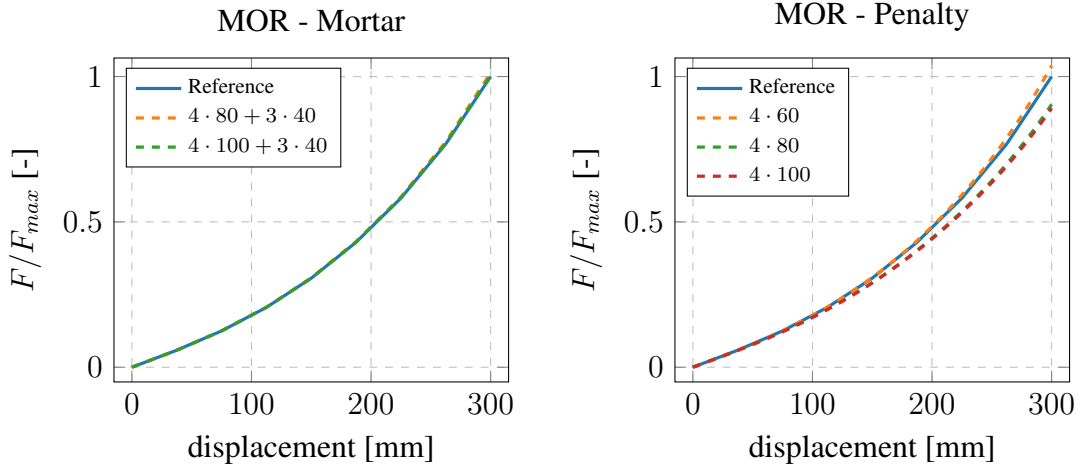


Figure 13: Force displacement curve of the "ring" example for the two different approaches that enforce the tied contact condition. The mortar approach is shown on the left and the penalty approach on the right.

In Figure 14 we show the force-displacement curves for the "omega" structure. Here, the reaction forces are overestimated for both the mortar MOR method and the penalty MOR method. The results of the mortar method are closer to the reference solution than the results of the penalty method. In the plot of the mortar MOR method, we analyze the influence of the inter-

face modes. It can be seen that by increasing the number of interface modes similar accuracies as an unreduced interface can be achieved.

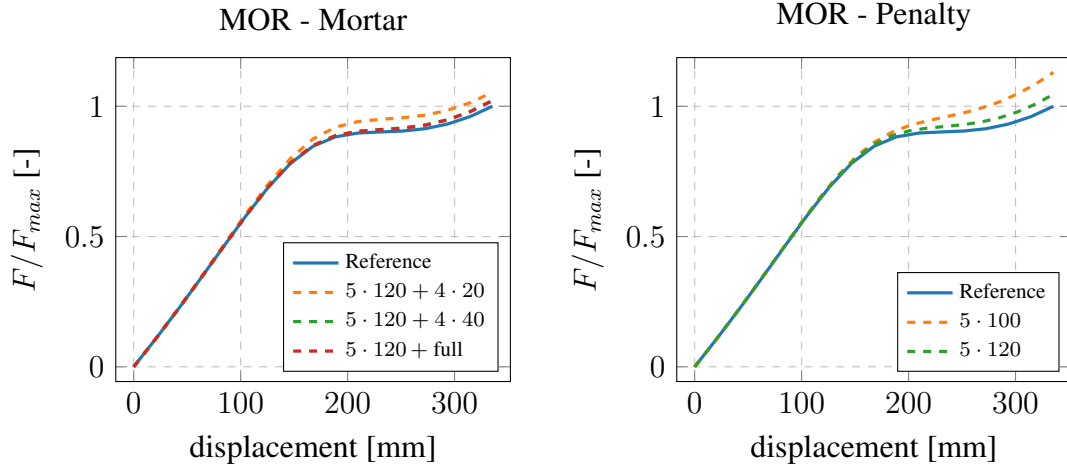


Figure 14: Force displacement curve of the omega-shaped example for the two different approaches that enforce the tied contact condition. The mortar approach is shown on the left and the penalty approach on the right.

In Figure 15 we show the relative simulation times regarding the total simulation time of the FOM. For the "ring" structure the simulation time is 8.95 % of the FOM time and for the "omega" structure it is 8.78 %. In Figure 15 we split the simulation times into two parts. Firstly, the assembly of the system and, secondly, the solution of the system. Most time savings were achieved in the solution of the system since the dimension of the ROM is smaller than the dimension of the FOM. Also, the assembly was more efficient in the ROM.

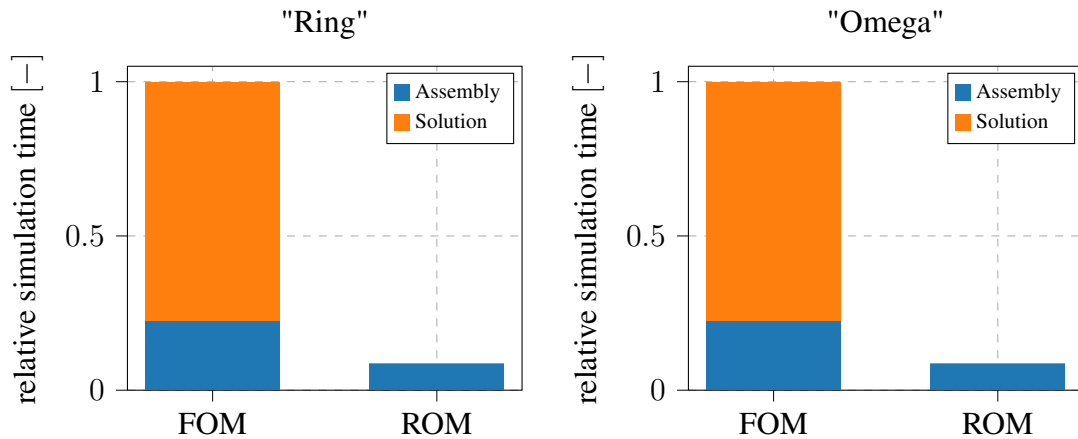


Figure 15: Normalized total time of the full order model (FOM) and the mortar reduced order model (ROM), for the "ring" example (left) and the "omega" example (right).

4.2.4 Viscoelasticity

In this section, we show that for inelastic material behavior, we can use the same modes as above. The modes are computed with a Neo-Hookean material (cf. Section 4.2.2) and are used now to reduce finite strain viscoelasticity. We simulated the "omega" boundary value problem now with a viscoelastic material law, according to Reese and Govindjee [1998]; Holthusen et al. [2023]. The displacement is applied over different time periods. The force-displacement curves in Figure 16 show the rate dependence of the reaction forces. The slower the displacement is applied, the smaller the reaction force.

The reduced computation is computed with 120 modes per substructure and 40 modes per interface. It can be seen that the nonlinear force-displacement curves are well-matched by the reduced solution. For the higher displacement rates the reduced solution differs more from the reference solution compared to smaller displacement rates.

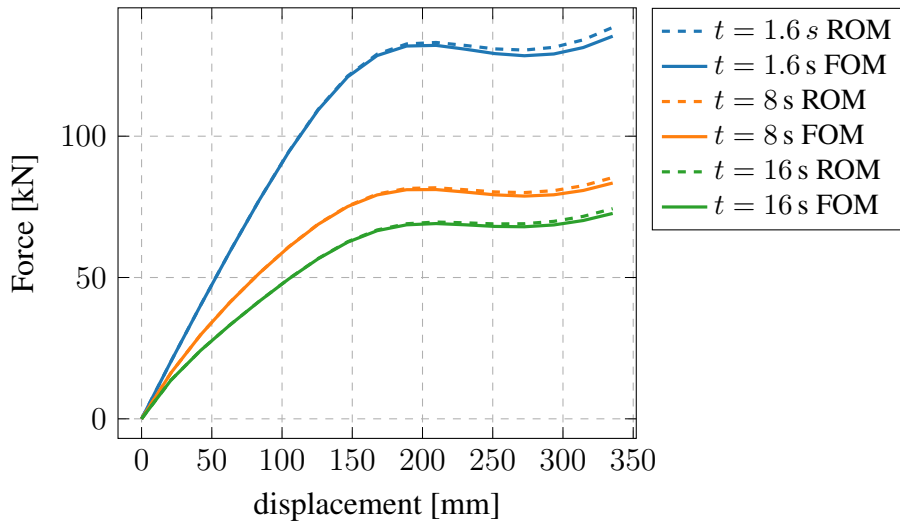


Figure 16: Force-displacement curves for different displacement rates considering finite strain viscoelasticity. The mortar approach is used for the reduced computation, with 120 modes per substructure and 40 modes per interface.

5 Discussion, conclusions and outlook

In this paper, we developed a substructuring technique using component-wise model order reduction and a mortar tied-contact formulation. In the numerical examples we demonstrated, that the developed method can predict solutions of systems constructed from reduced substructures. The method is capable of handling non-matching meshes, different stiffnesses, geometric non-linearities and material non-linearities (finite strain viscoelasticity). The POD modes used for

the substructure reduction were computed by simulating the substructures for different boundary conditions. We parametrized the boundary conditions on possible contact interfaces and used a randomized sampling procedure for the snapshot generation. New snapshots are only computed for boundary condition parameters where the solution cannot already be represented by the substructures POD-basis.

We also compared the mortar approach, where we removed the Lagrange multipliers by static condensation, to the penalty approach used in Zhou et al. [2018]. The mortar approach has multiple advantages compared to the penalty approach. The penalty approach has convergence problems for the here-discussed numerical examples. It also leads to ill-conditioned tangential stiffness matrices. We presume that the projection of this ill-conditioned tangential stiffness matrix leads to the observed convergence problems. Not for all penalty parameters a solution can be found and many more load steps are necessary compared to the mortar approach. The solution then also depends on the choice of the penalty parameter. The mortar approach does not have all these issues but has the disadvantage that the implementation is more complicated.

The here proposed method still depends on the original dimensions of the problem. In the future, we will incorporate hyperreduction methods into the method. Possible methods could be energy conserving sampling and weighting (ECSW) (Farhat et al. [2015]), or the discrete empirical interpolation method (DEIM) (Chaturantabut and Sorensen [2010]). The method can then also be applied to other nonlinear mechanical substructuring problems, e.g. structural dynamics or mechanical meta-materials. In the future, we will also address other material nonlinearities, such as damage and plasticity (e.g. Brepols et al. [2017]; Kehls et al. [2023]) Another further development would be to use optimization methods to find the optimal sampling points for the snapshot computation.

6 Acknowledgements

The authors gratefully acknowledge the funding granted by the German Research Foundation (DFG). The results presented here were developed within the subproject A01 of the Transregional Collaborative Research Center (CRC) Transregio (TRR) 280 with project number 417002380. Furthermore, T. Brepols, J. Kehls, and S. Reese gratefully acknowledge the funding that was granted within the subproject B05 "Coupling of intrusive and non-intrusive locally decomposed model order reduction techniques for rapid simulations of road systems" of the DFG CRC/TRR 339 with the project number 453596084, that was strongly involved in the origin of the paper. The authors acknowledge the work of Hagen Holthusen whose element and material implementations were included into the model order reduction finite element program.

References

- Benner, P., Gugercin, S. and Willcox, K. [2015], ‘A Survey of Projection-Based Model Reduction Methods for Parametric Dynamical Systems’, *SIAM Review* **57**(4), 483–531.
- Brepols, T., Wulfinghoff, S. and Reese, S. [2017], ‘Gradient-extended two-surface damage-plasticity: micromorphic formulation and numerical aspects’, *International Journal of Plasticity* **97**, 64–106.
- Bui, T. A., Park, J. and Kim, J.-S. [2024], ‘A reduced-order model for geometrically nonlinear curved beam structures with substructuring techniques’, *International Journal of Non-Linear Mechanics* **162**, 104724.
- Bui-Thanh, T., Willcox, K. and Ghattas, O. [2008], ‘Model Reduction for Large-Scale Systems with High-Dimensional Parametric Input Space’, *SIAM Journal on Scientific Computing* **30**(6), 3270–3288. Publisher: Society for Industrial and Applied Mathematics.
- Chaturantabut, S. and Sorensen, D. C. [2010], ‘Nonlinear Model Reduction via Discrete Empirical Interpolation’, *SIAM Journal on Scientific Computing* **32**(5), 2737–2764. Publisher: Society for Industrial and Applied Mathematics.
- Craig, R. R. and Bampton, M. C. C. [1968], ‘Coupling of substructures for dynamic analyses.’, *AIAA Journal* **6**(7), 1313–1319. Publisher: American Institute of Aeronautics and Astronautics.
- de Klerk, D., Rixen, D. J. and Voormeeren, S. N. [2008], ‘General Framework for Dynamic Substructuring: History, Review and Classification of Techniques’, *AIAA Journal* **46**(5), 1169–1181.
- Farhat, C., Chapman, T. and Avery, P. [2015], ‘Structure-preserving, stability, and accuracy properties of the energy-conserving sampling and weighting method for the hyper reduction of nonlinear finite element dynamic models’, *International Journal for Numerical Methods in Engineering* **102**(5), 1077–1110.
- Guo, T., Rokoš, O. and Veroy, K. [2024], ‘A reduced order model for geometrically parameterized two-scale simulations of elasto-plastic microstructures under large deformations’, *Computer Methods in Applied Mechanics and Engineering* **418**, 116467.
- Haasdonk, B. and Ohlberger, M. [2008], ‘Reduced basis method for finite volume approximations of parametrized linear evolution equations’, *ESAIM: Mathematical Modelling and Numerical Analysis* **42**(2), 277–302.
- Herkt, S., Dreßler, K. and Pinnau, R. [2009], ‘Model reduction of nonlinear problems in structural mechanics’.

- Hernández, J. A. [2020], ‘A multiscale method for periodic structures using domain decomposition and ECM-hyperreduction’, *Computer Methods in Applied Mechanics and Engineering* **368**, 113192.
- Hernández, J. A., Bravo, J. R. and Ares de Parga, S. [2024], ‘CECM: A continuous empirical cubature method with application to the dimensional hyperreduction of parameterized finite element models’, *Computer Methods in Applied Mechanics and Engineering* **418**, 116552.
- Hernández, J. A., Caicedo, M. A. and Ferrer, A. [2017], ‘Dimensional hyper-reduction of nonlinear finite element models via empirical cubature’, *Computer Methods in Applied Mechanics and Engineering* **313**, 687–722.
- Holthusen, H., Rothkranz, C., Lamm, L., Brepols, T. and Reese, S. [2023], ‘Inelastic material formulations based on a co-rotated intermediate configuration—application to bioengineered tissues’, *Journal of the Mechanics and Physics of Solids* **172**, 105174.
- Kehls, J., Kastian, S., Brepols, T. and Reese, S. [2023], ‘Reduced order modeling of structural problems with damage and plasticity’, *PAMM* **23**(4), e202300079.
- Kerschen, G., Golinval, J.-c., VAKAKIS, A. F. and BERGMAN, L. A. [2005], ‘The Method of Proper Orthogonal Decomposition for Dynamical Characterization and Order Reduction of Mechanical Systems: An Overview’, *Nonlinear Dynamics* **41**(1), 147–169.
- Kuether, R. J., Allen, M. S. and Hollkamp, J. J. [2016], ‘Modal Substructuring of Geometrically Nonlinear Finite-Element Models’, *AIAA Journal* **54**(2), 691–702.
- Kuether, R. J., Allen, M. S. and Hollkamp, J. J. [2017], ‘Modal Substructuring of Geometrically Nonlinear Finite Element Models with Interface Reduction’, *AIAA Journal* **55**(5), 1695–1706.
- Laursen, T. A., Puso, M. A. and Sanders, J. [2012], ‘Mortar contact formulations for deformable–deformable contact: Past contributions and new extensions for enriched and embedded interface formulations’, *Computer Methods in Applied Mechanics and Engineering* **205-208**, 3–15.
- McBane, S., Choi, Y. and Willcox, K. [2022], ‘Stress-constrained topology optimization of lattice-like structures using component-wise reduced order models’, *Computer Methods in Applied Mechanics and Engineering* **400**, 115525.
- Popp, A. and Wriggers, P., eds [2018], *Contact Modeling for Solids and Particles*, Vol. 585 of *CISM International Centre for Mechanical Sciences*, Springer International Publishing, Cham.
- Puso, M. A. [2004], ‘A 3D mortar method for solid mechanics’, *International Journal for Numerical Methods in Engineering* **59**(3), 315–336.

- Radermacher, A. and Reese, S. [2013], ‘Proper orthogonal decomposition-based model reduction for non-linear biomechanical analysis’, *International Journal of Materials Engineering Innovation* **4**(2), 149.
- Radermacher, A. and Reese, S. [2016], ‘POD-based model reduction with empirical interpolation applied to nonlinear elasticity’, *International Journal for Numerical Methods in Engineering* **107**(6), 477–495. [_eprint: https://onlinelibrary.wiley.com/doi/pdf/10.1002/nme.5177](https://onlinelibrary.wiley.com/doi/pdf/10.1002/nme.5177).
- Reese, S. and Govindjee, S. [1998], ‘A theory of finite viscoelasticity and numerical aspects’, *International Journal of Solids and Structures* **35**(26), 3455–3482.
- Ritzert, S., Macek, D., Simon, J.-W. and Reese, S. [2023], ‘An adaptive model order reduction technique for parameter-dependent modular structures’, *Computational Mechanics* .
- Rutzmoser, J. [2018], Model Order Reduction for Nonlinear Structural Dynamics, PhD thesis, Technische Universität München.
- Saad, Y. [2003], *Iterative methods for sparse linear systems*, SIAM.
- Scott, L. R. and Zhang, S. [1990], ‘Finite element interpolation of nonsmooth functions satisfying boundary conditions’, *Mathematics of computation* **54**(190), 483–493.
- Wenneker, F. [2013], Component Mode Synthesis for geometrically nonlinear structures, PhD thesis, Citeseer.
- Wohlmuth, B. I. [2001], *Discretization Methods and Iterative Solvers Based on Domain Decomposition*, Vol. 17 of *Lecture Notes in Computational Science and Engineering*, Springer Berlin Heidelberg, Berlin, Heidelberg.
- Wulfinghoff, S. [2024], ‘Statistically compatible hyper-reduction for computational homogenization’, *Computer Methods in Applied Mechanics and Engineering* **420**, 116744.
- Zhou, L., Simon, J.-W. and Reese, S. [2018], ‘Proper orthogonal decomposition for substructures in nonlinear finite element analysis: coupling by means of tied contact’, *Archive of Applied Mechanics* **88**(11), 1975–2001.